
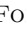



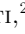






















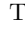



## The GLASS-JWST Early Release Science Program. II. Stage I release of NIRC*am* imaging and catalogs in the Abell 2744 region.

DIEGO PARIS <sup>1</sup>, EMILIANO MERLIN <sup>1</sup>, ADRIANO FONTANA <sup>1</sup>, ANDREA BONCHI <sup>2,1</sup>, GABRIEL BRAMMER <sup>3,4</sup>,  
MATTEO CORRENTI <sup>2,1</sup>, TOMMASO TREU <sup>5</sup>, KRISTAN BOYETT <sup>6,7</sup>, ANTONELLO CALABRÒ <sup>1</sup>, MARCO CASTELLANO <sup>1</sup>,  
WENLEI CHEN <sup>8</sup>, LILAN YANG <sup>9</sup>, K. GLAZEBROOK <sup>10</sup>, PATRICK KELLY <sup>8</sup>, ANTON M. KOEKEMOER <sup>11</sup>,  
NICHA LEETHOCHAWALIT <sup>12</sup>, SARA MASCIA <sup>1</sup>, CHARLOTTE MASON <sup>3,4</sup>, TAKAHIRO MORISHITA <sup>13</sup>,  
MARIO NONINO <sup>14</sup>, LAURA PENTERICCI <sup>1</sup>, GIANLUCA POLENTA <sup>2</sup>, GUIDO ROBERTS-BORSANI <sup>5</sup>, PAOLA SANTINI <sup>1</sup>,  
MICHELE TRENTI <sup>6,7</sup>, EROS VANZELLA <sup>15</sup>, BENEDETTA VULCANI <sup>16</sup>, ROGIER A. WINDHORST <sup>17</sup>,  
THEMIYA NANAYAKKARA <sup>10</sup> AND XIN WANG <sup>18,19,20</sup>

<sup>1</sup>*INAF Osservatorio Astronomico di Roma, Via Frascati 33, 00078 Monteporzio Catone, Rome, Italy*

<sup>2</sup>*Space Science Data Center, Italian Space Agency, via del Politecnico, 00133, Roma, Italy*

<sup>3</sup>*Cosmic Dawn Center (DAWN), Denmark*

<sup>4</sup>*Niels Bohr Institute, University of Copenhagen, Jagtvej 128, DK-2200 Copenhagen N, Denmark*

<sup>5</sup>*Department of Physics and Astronomy, University of California, Los Angeles, 430 Portola Plaza, Los Angeles, CA 90095, USA*

<sup>6</sup>*School of Physics, University of Melbourne, Parkville 3010, VIC, Australia*

<sup>7</sup>*ARC Centre of Excellence for All Sky Astrophysics in 3 Dimensions (ASTRO 3D), Australia*

<sup>8</sup>*Minnesota Institute for Astrophysics, University of Minnesota, 116 Church Street SE, Minneapolis, MN 55455, USA*

<sup>9</sup>*Kavli Institute for the Physics and Mathematics of the Universe, The University of Tokyo, Kashiwa, Japan 277-8583*

<sup>10</sup>*Centre for Astrophysics and Supercomputing, Swinburne University of Technology, PO Box 218, Hawthorn, VIC 3122, Australia*

<sup>11</sup>*Space Telescope Science Institute, 3700 San Martin Dr., Baltimore, MD 21218, USA*

<sup>12</sup>*National Astronomical Research Institute of Thailand (NARIT), Mae Rim, Chiang Mai, 50180, Thailand*

<sup>13</sup>*IPAC, California Institute of Technology, MC 314-6, 1200 E. California Boulevard, Pasadena, CA 91125, USA*

<sup>14</sup>*(INAF - Osservatorio Astronomico di Trieste, Via Tiepolo 11, I-34131 Trieste, Italy)*

<sup>15</sup>*INAF – OAS, Osservatorio di Astrofisica e Scienza dello Spazio di Bologna, via Gobetti 93/3, I-40129 Bologna, Italy*

<sup>16</sup>*INAF Osservatorio Astronomico di Padova, vicolo dell'Osservatorio 5, 35122 Padova, Italy*

<sup>17</sup>*School of Earth and Space Exploration, Arizona State University, Tempe, AZ 85287-1404, USA*

<sup>18</sup>*School of Astronomy and Space Science, University of Chinese Academy of Sciences (UCAS), Beijing 100049, China*

<sup>19</sup>*National Astronomical Observatories, Chinese Academy of Sciences, Beijing 100101, China*

<sup>20</sup>*Institute for Frontiers in Astronomy and Astrophysics, Beijing Normal University, Beijing 102206, China*

### ABSTRACT

We present images and a multi-wavelength photometric catalog based on all of the JWST NIRC*am* observations obtained to date in the region of the Abell 2744 galaxy cluster. These data come from three different programs, namely the GLASS-JWST Early Release Science Program, UNCOVER, and Director's Discretionary Time program 2756. The observed area in the NIRC*am* wide-band filters - covering the central and extended regions of the cluster, as well as new parallel fields - is 46.5 arcmin<sup>2</sup> in total. All images in eight bands (F090W, F115W, F150W, F200W, F277W, F356W, F410M, F444W) have been reduced adopting the latest calibration and references files available to date. Data reduction has been performed using an augmented version of the official JWST pipeline, with improvements aimed at removing or mitigating defects in the raw images and improve the background subtraction and photometric accuracy. We obtain a F444W-detected multi-band catalog including all NIRC*am* data and available HST data, adopting forced aperture photometry on PSF-matched images. The catalog is intended to enable early scientific investigations, and is optimized for the study of faint galaxies; it contains 24389 sources, with a 5 $\sigma$  limiting magnitude in the F444W band ranging from 28.5 AB to 30.5 AB, as a result of the varying exposure times of the surveys that observed the field. We

publicly release the reduced NIRCam images, associated multi-wavelength catalog, and code adopted for  $1/f$  noise removal with the aim of aiding users to familiarize themselves with JWST NIRCam data and identify suitable targets for follow-up observations.

*Keywords:* galaxies: high-redshift, galaxies: photometry

## 1. INTRODUCTION

In just a few months of observations, JWST has demonstrated its revolutionary scientific capabilities. Early observations have shown that its performance is equal or better than expected, with image quality and overall efficiency that match or surpass pre-launch estimates (Rigby et al. 2022). Publicly available datasets obtained by the Early Release Observations and Early Release Science programs have already enabled a large number of publications based on JWST data, ranging from exoplanets to the distant Universe.

In particular, a number of works exploited the power of NIRCAM to gather the first sizeable sample of candidates at  $z \geq 10$  (e.g., Castellano et al. 2022a; Donnan et al. 2023; Finkelstein et al. 2022; Morishita & Stivavelli 2022; Naidu et al. 2022; Yan et al. 2022; Roberts-Borsani et al. 2022; Robertson et al. 2022; Castellano et al. 2022b; Bouwens et al. 2022), showing the power of JWST in exploring the Universe during the re-ionization epoch.

In this paper we present the full data set obtained with NIRCam in the region of the  $z = 0.308$  cluster Abell 2744 that will significantly expand the available area for deep extragalactic observations. The central region of the cluster, with the assistance of lensing magnification, allows an insight into the distant Universe at depth and resolution superior of those of NIRCam in blank fields. The data set analyzed here are obtained through three public programs: i) GLASS-JWST ERS (Treu et al. 2022), ii) UNCOVER (Bezanson et al. 2022), and iii) Director’s Discretionary Time Program 2756, aimed at following up a Supernova discovered in GLASS-JWST NIRISS imaging. We have analyzed and combined the imaging data of all these programs and obtained a multi-wavelength catalog of the objects detected in the F444W band.

In order to facilitate exploitation of these data, we release reduced images and associated catalog on our website and through the Mikulski Archives for Space Telescopes (MAST). This release fulfills and exceeds the requirements of the Stage I data release planned as part of the GLASS-JWST program. It is anticipated that a final (Stage II) release will follow in approximately a year, combining additional images scheduled in 2023, and taking advantage of future improvements in data processing and calibrations.

This paper is organized as follows. In Section 2 we present the data-set and discuss the image processing pipeline. In Section 3 the methods applied for the detection of the sources and the photometric techniques used to compute the fluxes are presented. Finally in Section 4 we summarize the results. Throughout the paper we adopt AB magnitudes (Oke & Gunn 1983).

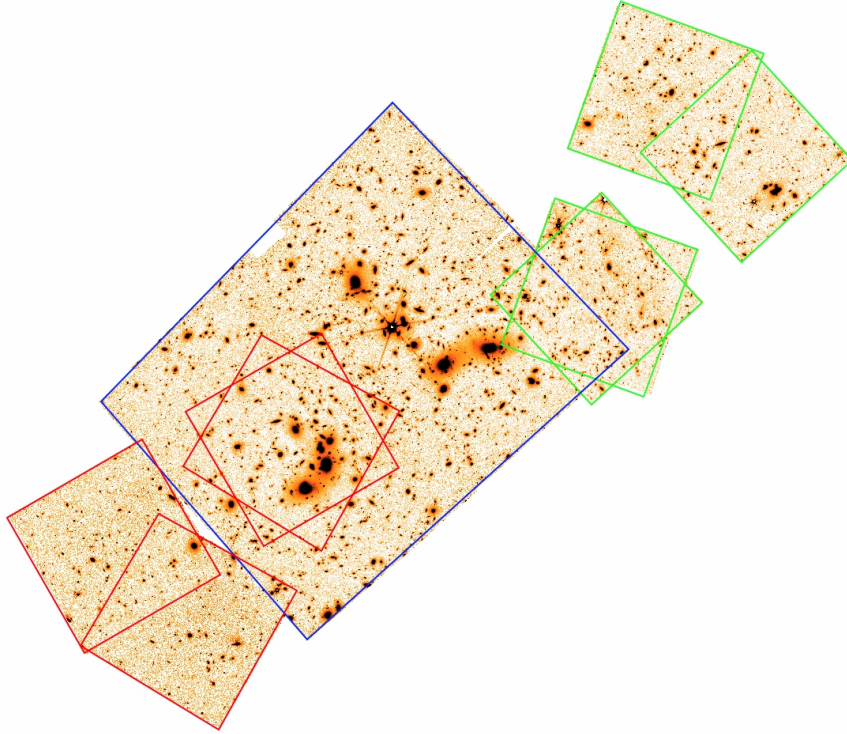
## 2. DATA REDUCTION

### 2.1. Data Set

The NIRCam data analyzed in this paper are taken from three programs that targeted the  $z = 0.308$  cluster Abell 2744 (A2744 hereafter) and its surroundings. The first set of NIRCam images were taken as part of the GLASS-JWST survey (Treu et al. 2022, hereafter T22), in parallel to primary NIRISS observations on June 28–29 2022 and to NIRSpec observations on Nov. 10–11, 2022. We refer to these data sets as GLASS1 and GLASS2, or collectively as GLASS, both of which consist of imaging in seven broad-band filters from F090W to F444W (see Treu et al. 2022 for details). We note that the final pointing is different from the scheduled one presented by Treu et al. (2022) due to the adoption of an alternate position angle (PA) during the NIRSpec spectroscopic observations. As the primary spectroscopic target was the A2744 cluster, these parallel images are offset to the North-West. By virtue of the long exposure times, these images are the deepest presented here.

The second set of NIRCam observations considered here were taken as part of the UNCOVER program (Bezanson et al. 2022), which targets the center of the A2744 cluster and the immediate surroundings. These images are composed of four pointings and result in a relatively homogeneous depth, as discussed below. They were taken on November 2-4-7 and 15, and adopt the same filter set as GLASS-JWST, except for the adoption of the F410M filter instead of F090W.

Finally, NIRCam imaging of the A2744 center was also obtained as part of DDT program 2756 (PI W. Chen, DDT hereafter) on October 20 and December 6 2022 (UT). These two data sets are dubbed DDT1 and DDT2 hereafter. The DDT filter set is the same as GLASS-JWST with the exception of the F090W filter, and overall shorter exposure times. One of the two NIRCam modules overlaps with UNCOVER.



**Figure 1.** Full view of the F444W mosaics. Colored boxes show the position of the three different data sets used here: GLASS (green), UNCOVER (blue) and DDT (red). The entire image (including the empty space) is approximately  $12.7 \times 10.9$  arc minutes wide.

In Table 1 we list the exposure times adopted in the various filters for each of the aforementioned programs, while the footprints of the fields are illustrated in Figure 1.

As a result of the overlap between programs and of their different observation strategies, the resulting exposure map is complex and inhomogeneous across bands and area. An analysis of the depth resulting from this exposure map is reported below.

## 2.2. Data reduction

### 2.2.1. Pre-reduction steps

Image pre-reduction was executed using the official JWST calibration pipeline, provided by the Space Telescope Science Institute (STScI) as a Python software suite<sup>1</sup>. We adopted Version 1.8.2 of the pipeline and Versions between `cjwst_1014.pmap` and `cjwst_1019.pmap` of the CRDS files (the only changes between these versions is the astrometric calibration, that is dealt with as described below). We executed the first two stages of the pipeline (i.e. `calwebb_detector1` and

**Table 1.** NIRCам Exposure time

Filter	GLASS1	GLASS2	DDT1/2	UNCOVER
F090W	11520	16492	-	-
F115W	11520	16492	2104	10822
F150W	6120	8246	2104	10822
F200W	5400	8246	2104	6700
F277W	5400	8246	2104	6700
F356W	6120	8246	2104	6700
F410M	-	-	-	6700
F444W	23400	32983	2104	8246

NOTE—Exposure time (in seconds) for each pointing of the three programs considered here.

`calwebb_image2`), adopting the optimized parameters for the NIRCам imaging mode, that convert single detector raw images into photometric calibrated images.

Using the first pipeline stage `calwebb_detector1` we processed the raw uncalibrated data (`uncal.fits`) in order to apply detector-level corrections performed on a group-by-group basis, as dark subtractions, reference pixels corrections, non-linearity corrections and jump

<sup>1</sup> <https://jwst-pipeline.readthedocs.io/en/latest/jwst/introduction.html>

detection that allows to identify cosmic rays (CR) events on the single groups. The last step of this pipeline stage allows us to derive the mean count rate, in units of counts per second, for each pixel by performing a linear fit to the data in the input image (the so-called ramp-fitting) excluding the group masked due to the identification of a cosmic ray jump.

The output files of the previous steps (`rate.fits`) are processed through the second pipeline stage `calwebb_image2`, which consists of additional instrument-level and observing-mode corrections and calibrations, as the geometric-distortion correction, the flat-fielding, and the photometric calibrations that converting the data from units of countrate to surface brightness (i.e. MJy per steradian) generates a fully calibrated exposure (`cal.fits`).

The `cal.fits` file contains also an RMS layer, which combines the contribution of all pixel noise sources, and a DQ mask where the first bit (`DO_NOT_USE`) identifies pixels that should not be used during the resampling phase.

We then applied a number of custom procedures to remove instrumental defects that are not dealt with the STScI pipeline. Some of them have already been adopted in (Merlin et al. 2022, hereafter M22) and described there: we illustrate below only the major changes to the STScI pipeline in default configuration and/or to the procedure adopted in M22.

- “*Snowballs*”, i.e. circular artifacts observed in the in-flight data caused by a large cosmic ray impacts. Those hits leave a bright ring-shaped defect in the image since the affected pixels are just partially identified and masked. In M22, we developed a technique to fully mask out these features, which was not necessary here. Indeed, version 1.8.1 of the JWST pipeline introduced the option to identify snowball events, expanding the typical masking area to include all the pixels affected. This new implementation provides the opportunity to correct these artifacts directly at the ramp fitting stage, at the cost of a larger noise on the corresponding pixels. We activated this non-default option, and fine tuned the corresponding parameters to completely mask all the observed snowballs and, at the same time, minimize the size of high noise areas.
- “*NL Mask*”, on `cal` images of the NIRCcam Module B Long Wavelength detector are visible bright groups of pixels not well corrected during pre-reduction. These pixels are more evident on deeper pointing and are identified as “well not defined”

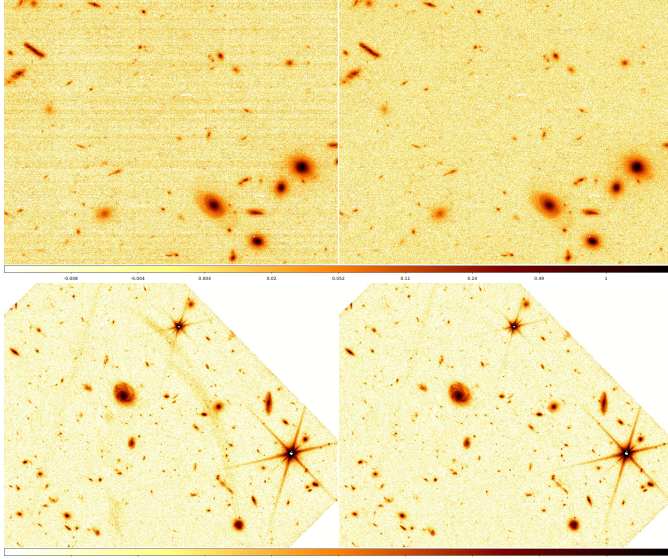
pixels<sup>2</sup> in the Non Linearity Calibration file<sup>3</sup>. We selected those pixels and masked them as `DO_NOT_USE` to not to be used during stacking phase.

- *1/f noise*, which introduces random vertical and horizontal stripes into the images (see Schlawin et al. 2020). We remove this by subtracting the median value from each line/column, after masking out all objects and bad pixels. The masks were obtained by running SEXTRACTOR (Version 2.25.0) (Bertin & Arnouts 1996) and then dilating the resulting segmentation image, applying a differential procedure to dilate objects depending on their ISOAREA: the segmentation of objects with  $\text{ISOAREA} < 5000$  pixels was dilated using a  $3 \times 3$  convolution kernel and a dilation of 15 pixels, while for the segmentation of objects with  $\text{ISOAREA} \geq 5000$  pixels a  $9 \times 9$  convolution kernel and a dilation of  $4 \times 15$  pixels was used. The procedure was executed separately for each amplifier in the SW detectors (i.e. 4 times for each individual image) with the exception of the denser areas corresponding to the centers of the clusters and the brightest field star, where objects are significantly larger than the amplifier width (500 pixels, corresponding to about  $30''$ ) and could not be masked efficiently. In this case we removed the  $1/f$  noise over the entire row. As this extension of the STScI pipeline could be useful for other programs, we publicly release the code adopted for this step.
- *Scattered light*: we identify additive features in the F115W, F150W and F200W images. These low-surface brightness features have already been revealed by commissioning data (see Rigby et al. 2022) and are due to scattered light entering into optical path. These anomalies have been dubbed *wisps* or *claws*, depending on their origin and morphology. *Wisps* have a nearly constant shape and a template pattern is available for subtraction from the images. We removed these features by extracting their 2D profile from the available template (we do not use the entire template image to avoid subtracting its empty but noisy regions) and then normalizing the residual template to match the feature intensity in each image. *Claws* have been first identified and singled out in images.

<sup>2</sup> [https://www.stsci.edu/files/live/sites/www/files/home/jwst/documentation/technical-documents/\\_documents/JWST-STScI-004714.pdf](https://www.stsci.edu/files/live/sites/www/files/home/jwst/documentation/technical-documents/_documents/JWST-STScI-004714.pdf)

<sup>3</sup> [https://jwst-crds.stsci.edu/browse/jwst\\_nircam\\_linearity\\_0011.rmap](https://jwst-crds.stsci.edu/browse/jwst_nircam_linearity_0011.rmap)





**Figure 2.** Examples of custom procedures to remove residual instrumental defects, not dealt with the current STScI pipeline. *Top:* 1/f stripes removal on a GLASS F200W single exposure. *Bottom:* A portion of the GLASS F150W mosaic before and after the claws treatment.

Their shape on each image has been reconstructed by interpolating a 2D mesh with box size 32 pixels and then eventually subtracted from the same image. We find that these procedures efficiently remove most of these features, as shown in Figure 2.

Other defects were found in the F090W image, and to a lesser extent in the F115W one, which are due to a so-called “wing-tilt event” that happened during the observations. These defects have been masked as in M22.

We then re-scaled the single exposures to units of  $\mu\text{Jy}/\text{pixel}$ , using the conversion factors output by the pipeline.

### 2.2.2. Astrometry

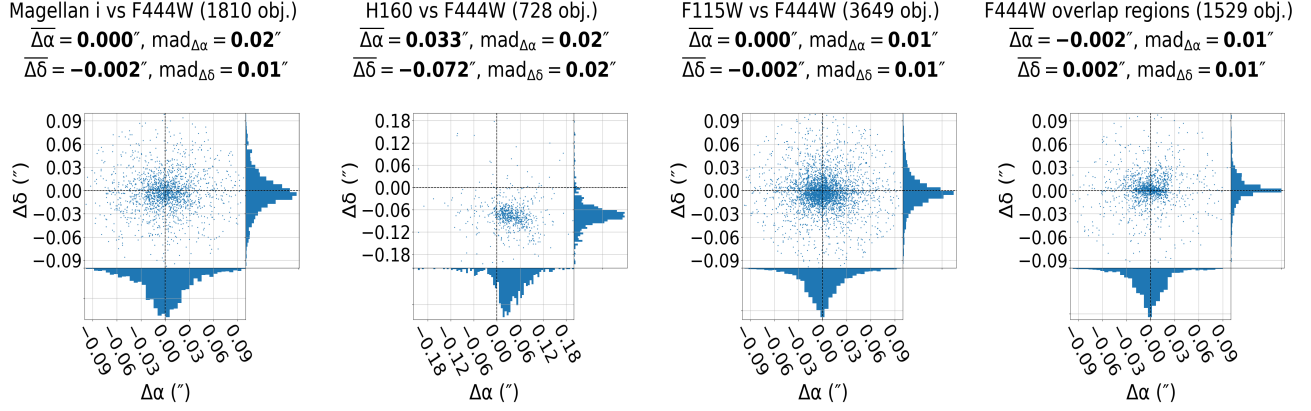
The astrometric calibration was performed using SCAMP (Bertin 2006), with 3rd order distortion corrections (PV coefficients up to  $j = 10$ ). At variance with the procedure we adopted in M22, we started from the distortion coefficient computed by the STScI pipeline and stored in the `cal` images, and refine the astrometric solution by running SCAMP in `cal` mode, which optimizes the solution with limited variations from the starting solution. We have found this procedure both accurate and reliable, as described below. We first obtained a global astrometric solution for the F444W image, which is usually the deepest, tied to a ground-based catalog obtained in the *i*-band with the Magellan telescope in good see-

ing condition (see T22 for details) of the same region, which had been previously aligned to GAIA-DR3 stars (Gaia Collaboration et al. 2016, 2022 in prep.). We then took the resulting high-resolution catalog in F444W as reference for the other JWST bands, using compact, isolated sources detected at high signal-to-noise at all wavelengths. Each NIRCcam detector has been analysed independently, in order to simplify the treatment of distortions and minimise the offsets of the sources in different exposures. Finally, we used SWARP (Bertin et al. 2002) to combine the single exposures into mosaics projected onto a common aligned grid of pixels, and SExtractor to further clean the images by subtracting the residual sky background. The pixel scale of all the images was set to  $0.031''$  (the approximate native value of the short wavelength bands), to allow for simple processing with photometric algorithms.

The final image, computed as a weighted stack of all the images from the three programs, has a size of  $24397 \times 21040$  pixels, corresponding to  $12.6 \times 10.87$  arcmin<sup>2</sup>. In this frame, the area covered by the wide-band NIRCcam images (F115W, F150W, F200W, F277W, F356W and F444W) is of exactly 46.5 arcmin<sup>2</sup>. The F444W image is shown in Figure 1.

Given the especially deep and sharp nature of the JWST images, where most of the faint objects have sizes below  $0.5''$ , the requirements on the final astrometric accuracy are extremely tight, to avoid errors in the multi-band photometry (where a displacement of as little as  $0.1''$  can bias color estimates). These requirements must be met also in the overlapping regions of the various surveys, which have often been observed with different detectors.

To verify the final astrometric solution we conducted a number of validation tests, where we compare the positions of cross-matched objects in catalogues extracted from different images. For each of these catalogues we used SExtractor in single image mode and adopted the XWIN and YWIN estimators of the object center, which are more accurate than other choices. At the unprecedented image quality of NIRCcam, the accurate center of extra-galactic objects with complex morphology may be difficult to estimate with high accuracy, especially when observed across a large wavelength interval. To minimize errors, we limited the comparison to objects with well defined positions, using the  $\Delta X, \Delta Y = \text{ERRAWIN\_WORLD}, \text{ERRBWIN\_WORLD}$  estimators of the error and limiting the analysis to objects with  $(\Delta X^2 + \Delta Y^2)^{1/2} \leq 0.018''$ . From these catalogues we estimated both the average offset of the object centers  $\overline{\Delta\alpha}$  and  $\overline{\Delta\delta}$ , and the median average deviation  $\text{mad}_\alpha$  and  $\text{mad}_\delta$ , which measure the



**Figure 3.** Validation tests on the astrometric registration. *Left:* scatter diagram reporting the displacement  $\delta RA$  and  $\delta DEC$  of sources between the Magellan  $i$ -band catalog registered to Gaia DR3 used as global reference for calibration and the final F444W NIRCcam catalog. *Middle left:* As above, applied to the scatter between the AstroDeep catalog and the final F444W NIRCcam catalog obtained on the central region of the A2744 cluster, as obtained in the context of the Frontier Fields initiative (Merlin et al. 2016a). *Middle right:* Offset between the position of sources in the F444W and the F115W images. *Right:* Positional offset between the objects detected in the UNCOVER-only images and those in the GLASS and DDT samples, on two overlapping regions. In all diagrams the average value  $\Delta\alpha$  and  $\Delta\delta$  and the median average deviation  $mad_{\Delta\alpha}$  and  $mad_{\Delta\delta}$  are reported.

intrinsic scatter in the alignment. In Figure 3 we report the main outcome of these tests:

- (*Left*) We first compared the positions of objects in the original Magellan  $i$ -band and the resulting F444W of the entire mosaic. We find an essentially zero offset and  $mad_{\alpha} \simeq mad_{\delta} \simeq 0.02''$ , which is 2/3 of a pixel.
- (*Middle left*) We compared the F444W catalog with the AstroDeep  $H_{160}$  catalog obtained on the central region of the A2744 cluster, as obtained in the context of the Frontier Fields initiative (Merlin et al. 2016a). While the intrinsic scatter is still good ( $mad_{\alpha} \simeq mad_{\delta} \simeq 0.02''$ ), we find a systematic offset by about 1 pixel in RA and 2.5 pixels in DEC, which is most likely due to different choices in the absolute calibration of the ACS/WFC3 data released within the Frontier Fields.
- (*Middle right*) We compare here the relative calibration of filters at the two extremes of the spectral range, F444W and F115W, where morphological variations and color terms may change the center position and affect the astrometric procedure. We find again very good alignment with negligible offset and small  $mad_{\alpha} \simeq mad_{\delta} \simeq 0.01''$ .
- (*Right*) Finally, we compare the astrometric solutions on the overlapping areas by summing independently the data of the three different programs and checking the accuracy in the overlapping area.

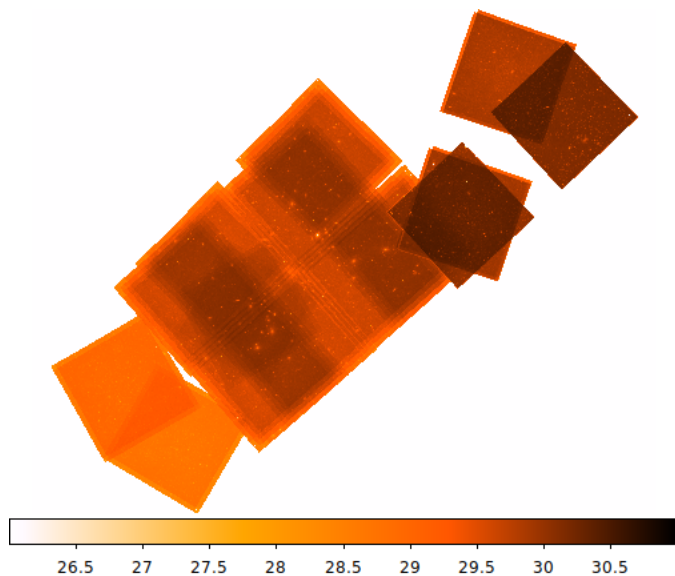
Again we find very good alignment with negligible offset and small  $mad_{\alpha} \simeq mad_{\delta} \simeq 0.01''$ .

We therefore conclude that the astrometric procedure is accurate and adequate to the goals of this Stage I release. In the future we plan to further explore and validate other options for astrometric registration and also release images with a smaller pixel scale, to better exploit the unprecedented image quality of the JWST data. We note that the GLASS-JWST data have a very limited dithering pattern (which was driven by spectroscopic requirements) and so may benefit only marginally from moving to smaller pixels.

### 2.3. Estimating the Final Depth

The final coaddition of the different images is weighted according to their depth, as estimated by the RMS image produced by the pipeline. We therefore obtain an optimally averaged image with the resulting RMS image. We *a posteriori* verified whether the noise estimate encoded in the RMS effectively reproduced the photometric noise. To do this, we injected artificial point sources of known magnitude in empty regions of the image, and measured their fluxes and uncertainties with A-PHOT (Merlin et al. 2019), using apertures of radius  $0.1''$ . To take into account the fact that the mosaics are the result of a complex pattern of different exposures, we divided the maps into regions of similar total exposure time, and performed this analysis separately in each region.

In general, we find that the RMS of the resulting flux distribution is  $1.1\times$  larger than the value we would ex-



**Figure 4.** Depth of the full mosaic F444W image, as produced by our pipeline on the basis of the variance image of each exposure and with the re-normalization described in the text. Each pixel has been converted into  $5\sigma$  limiting flux computed on a circular aperture of  $0.2''$ .

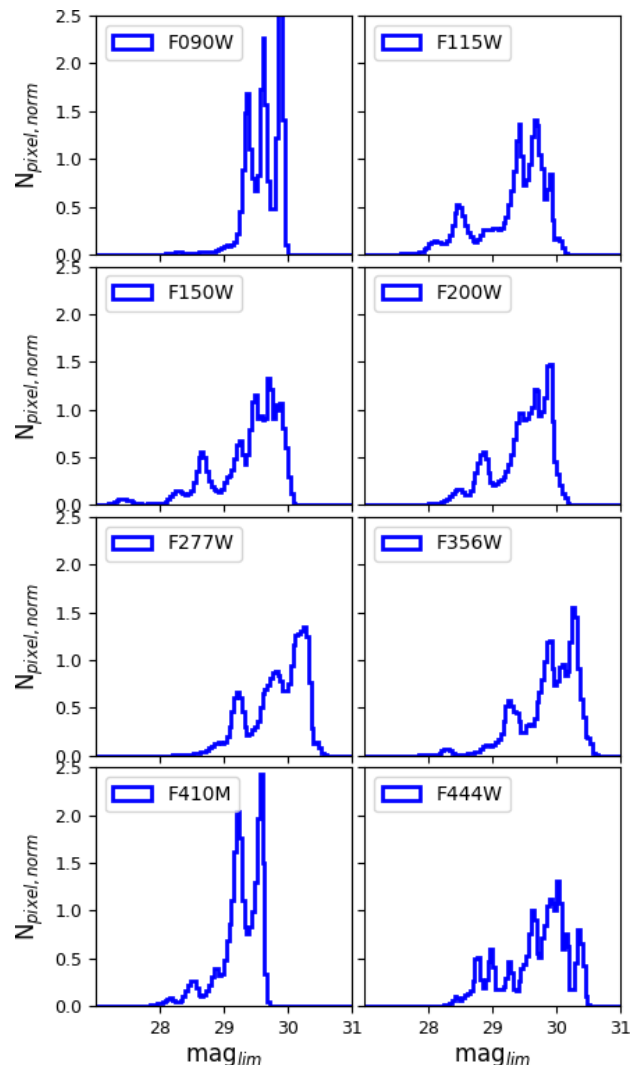
pect from the SEXTRACTOR errors, which are computed from the RMS image. A larger difference ( $1.4\times$ ) is found for the F444W GLASS image, which is affected by a residual pattern due to poor flat-fielding with the current calibration data. We therefore re-scaled the RMS maps produced by the pipeline according to these factors.

The resulting depth of this procedure is shown in Figure 4. The RMS image is converted into a  $5\sigma$  limiting flux computed on a circular aperture with a diameter of  $0.2''$ , that is the size adopted to estimate colors of faint sources. The depth ranges from  $\simeq 28.6$  AB on the DDT2 footprint (in particular the area not overlapping with DDT1) to  $\simeq 30.2$  AB in the area where GLASS1 and GLASS2 overlap, arguably one of the deepest images obtained so far by JWST.

A more quantitative assessment of the depth in the various filters is reported in Figure 5, where we show the distribution of the limiting magnitudes in each image resulting from the different strategies adopted by the surveys, computed as described above. A clear pattern is seen, illustrating the large, mid-depth area obtained by UNCOVER and the shallower and deeper parts obtained by DDT and GLASS respectively.

#### 2.4. HST Imaging

We have also used the existing images obtained with HST in previous programs, namely with the F435W, F606W, F775W and F814W bands with ACS and the



**Figure 5.** Distribution of the limiting magnitude for each band, as shown in the legend. Limiting magnitudes per pixel have been computed as for Figure 4.

F105W, F125W, F140W and F160W bands with WFC3 - other HST data are available from MAST but are either too shallow and/or limited in area and are not considered here. Among these data are included also the images that we obtained with DDT Program HST-GO-17231 (PI: Treu), which was specifically aimed at obtaining ACS coverage for the majority of the GLASS1 and GLASS 2 fields. We have used calibrated stacked image and weights (G. Brammer, private communication) that we have realigned (after checking that the astrometric solution is consistent) onto our reference grid to allow a straightforward computation of colors.

### 3. PHOTOMETRIC CATALOG

#### 3.1. Detection



We follow here the same prescriptions adopted by M22 and Castellano et al. (2022a,b). We performed source detections on the F444W band, since it is generally the deepest or among the deepest image for each data set, and because high-redshift sources (which are the main focus of these observations) are typically brighter at longer wavelengths. This approach has the advantage of delivering a clear-cut criterion for the object detections, that can easily be translated into a cut of rest-frame properties for high redshift sources.

We used SEXTRACTOR, adopting a double-pass object detection as applied for the HST-CANDELS campaign (see Galametz et al. 2013), to detect the objects, following the recipes and parameters described in M22. We note in particular that we adopt a detection threshold corresponding to a signal-to-noise ratio (SNR) of 2. This is based on simulations, as discussed in M22. The other SEXTRACTOR parameters used are listed in M22.

The final SEXTRACTOR catalogue on the entire A2744 area contains 24389 objects.

Estimating the completeness and purity in a patchy (in terms of area and exposure) mosaic derived from the large number of observations adopted here, is intrinsically ambiguous. As shown in Figure 5 the depth of these images spans approximately 2 magnitudes, and the completeness is therefore inhomogeneous - not to mention the existence of the cluster that complicates both the detection and the estimate of the foreground volume (C22b). For these reasons, we do not attempt the traditional estimate of the completeness and refer to Figure 4 and to Figure 5 for an evaluation of the depth. For a proper analysis of the completeness we refer the reader to the methodology adopted by C22b where we estimate the completeness separately on the individual mosaics of the three data sets, which were processed independently. We make the three mosaics available upon request for this purpose.

### 3.2. Photometry

We have compiled a multi-wavelength photometric catalog following again the prescriptions of M22, which in turn is based on previous experience with Hubble Space Telescope (HST) images in CANDELS (see e.g. Galametz et al. 2013) and in AstroDeep (Merlin et al. 2016b, 2021). The catalog is based on a detection performed on the F444W image described above, and PSF-matched aperture photometry of all the sources. We include all the NIRCcam images presented here and existing images obtained with HST in previous programs, namely with the F435W, F606W, F775W and F814W bands with ACS and the F105W, F125W, F140W and F160W bands with WFC3.

The images considered here have PSFs that range from 0.035" to 0.2". Considering that most of the objects have small sizes, with half-light-radii less than 0.2", it is necessary to apply a PSF homogenization to avoid bias in the derivation of color across the spectral range.

#### 3.2.1. PSF matching

Since the detection band is the one with the coarsest resolution, we PSF-matched all the other NIRCcam images to it for color fidelity. We created convolution kernels using the WEBBPSF models publicly provided by STScI<sup>4</sup>, combining them with a Wiener filtering algorithm based on the one described in Boucaud et al. (2016); and we used a customised version of the convolution module in T-PHOT (Merlin et al. 2015, 2016a), which uses FFTW3 libraries, to smooth the images. This approach delivers consistent results with those obtained using the software GALIGHT (Ding et al. 2020). We note that this approach is inevitably approximated. The JWST PSF is time- and position-dependent (Nardiello et al. 2022), and our dataset is the inhomogeneous combination of data obtained at different times and with different PA, so that the PSF definitely changes over the field. For this version of the catalog we used the Uncover PSF models as average PSFs, and we plan to improve our PSF estimation in the future versions of the catalog that will be released in Stage II.

Similarly, concerning the HST images, we note that all of them have too few stars to obtain a robust estimate of the PSF directly from the images, so that we adopt in all cases existing HST PSFs, taken from CANDELS. This approximation may introduce small biases in the final catalog. ACS images have been PSF-matched to F444W, while for the WFC3 F105W, F125W, F140W and F160W images, which have a PSF larger than the F444W one, we have done the inverse - smoothed the F444W image and the WFC3 F105W, F125W, F140W to the F160W and followed a slightly different procedure that we describe below.

#### 3.2.2. Flux estimate

The total flux is measured with A-PHOT on the detection image F444W by means of a Kron elliptical aperture (Kron 1980). As we have shown in M22, simulations suggest that Kron fluxes measured with A-PHOT are somewhat less affected by systematic errors, while being slightly more noisy.

<sup>4</sup> <https://jwst-docs.stsci.edu/jwst-near-infrared-camera/nircam-predicted-performance/nircam-point-spread-functions>



Then, we used A-PHOT to measure the fluxes at the positions of the detected sources on the PSF-matched images, masking neighboring objects using the SEXTRACTOR segmentation map. Given the wide range of magnitudes and sizes of the target galaxies we have measured the flux in a range of apertures: the segmentation area (the images being on the same grid and PSF-matched) and five circular apertures with diameters that are integer multiples ( $2\times, 3\times, 8\times, 16\times, \dots$ ) of the FWHM in the F444W band, that correspond to  $0.28''$ ,  $0.42''$ ,  $1.12''$  and  $2.24''$  diameters. For the four WFC3 images (which have a PSF larger than F444W) we first filtered the F444W to their FWHM and then measured colors between the filtered F444W and the WFC3 images. To minimize biases when these colors are combined with those of the other bands, we use in this case apertures the same multiples of the WFC3 PSF adopted for the other bands. We remark that this procedure is only approximate, and delivers a first order correction of the systematic effects due to different PSFs. In a future release we plan to adopt more sophisticated approaches to optimize photometry, including but not limited to the improvement of the PSF estimate and applying T-PHOT on WFC3 images that have a larger PSF.

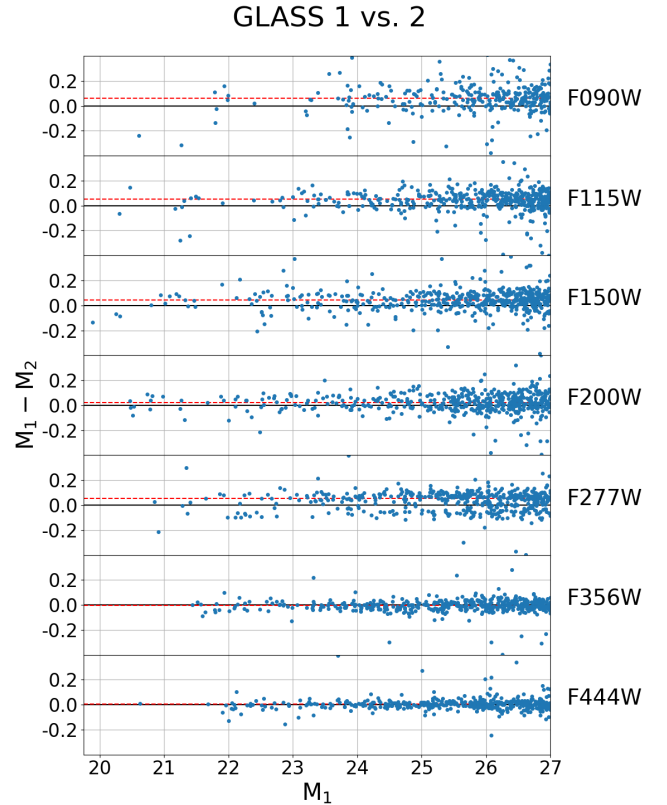
Total fluxes are obtained in the other bands by normalizing the colors in a given aperture to the F444W total flux, i.e. by computing  $f_{m,total} = f_{m,aper} / f_{F444W,aper} \times f_{F444W,total}$ , as described in M22.

We release the five catalogues described above (one computed on segmentation and four on the different apertures) and we leave the user to choose which is the most suitable for a given science application. In general small-aperture catalogues are more appropriate for faint sources as they match their small sizes and minimize deblending. Larger apertures may be more appropriate for brighter sources and especially cluster members.

### 3.2.3. Validation tests

We have performed a few validation tests to verify primarily the flux calibration, that has been the subject of many revisions in these first months, and to a lesser extent of the procedure adopted to derive the photometric catalog.

The overlap between GLASS1 and GLASS2 southern quadrants offers us a nice opportunity to test the NIRC-Cam flux calibration. Indeed, the two GLASS observations have been observed in two epochs (July and October 2022) with a PA difference of nearly 150 degrees. As a result, the southern quadrant of GLASS1 and GLASS2 are largely overlapping but have been observed with modules B and A, respectively. We have therefore obtained stacked images of the two epochs separately, built



**Figure 6.** Stability of the photometric calibration between different detectors, as measured by comparing the photometry of high S/N objects ( $S/N > 25$ ) detected in the two epochs of observations in the SE quadrant of GLASS (lower leftmost green square in Figure 1). Objects in this area have been observed in two epochs (July and October 2022) and with modules B and A, respectively. For each filter difference in magnitude  $\Delta M = M_1 - M_2$  for objects between epoch1 and epoch2 as a function of  $M_1$  is reported. Red dashed lines represent the median offsets, namely we found:  $\overline{\Delta M} \approx 0.06$  with  $mad \approx 0.05$  for F090W,  $\overline{\Delta M} \approx 0.05$  with  $mad \approx 0.04$  for F115W,  $\overline{\Delta M} \approx 0.04$  with  $mad \approx 0.04$  for F150W,  $\overline{\Delta M} \approx 0.02$  with  $mad \approx 0.04$  for F200W,  $\overline{\Delta M} \approx 0.05$  with  $mad \approx 0.04$  for F277W, and negligible in F356W and F444W with  $mad \approx 0.03$  and  $mad \approx 0.02$  respectively. We have visually inspected the bright objects with  $|\Delta M| > 0.05$  and verified that they mostly originate from saturated stars or objects with incomplete coverage.

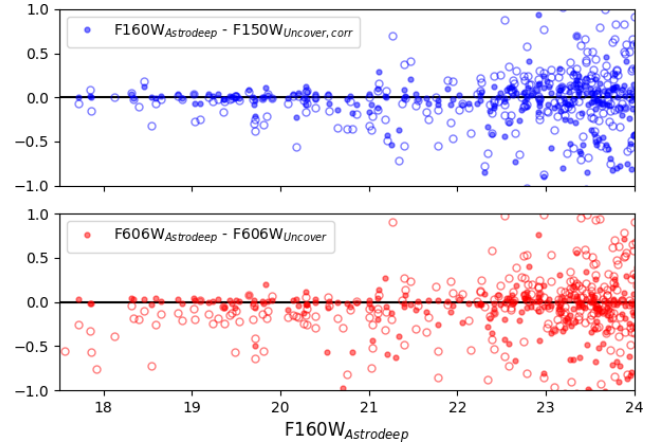
a photometric catalog with the same recipes and checked the magnitude difference between objects observed with different detectors. The result of this exercise, that has been done on all bands, is reported in Figure 6. We note that in the short bands the two modules are made of 4 detectors, each with an independent calibration, that we plot all together in Figure 6. The comparison, that is limited to objects observed with high  $S/N > 25$ , shows that the average magnitude difference between the two

modules is in general quite small, in all cases below 0.05 *mags* (see Figure 6 and its captions for details). This confirms that the flux calibration between the different modules is reasonably stable at this stage.

As a further check to validate the photometric pipeline, we have compared the  $m_{606}$  and  $m_{150}$  magnitudes for the sources in the core of the A2744 cluster with those measured in the same F606W and in the nearby F160W bands measured on HST images, that we published within the AstroDeep project (Merlin et al. 2016b; Castellano et al. 2016). This comparison is shown in Figure 7. Magnitudes in the NIRCам F150W band have been shifted by  $\simeq 0.05$  in order to correct for the small bandpass difference: the term was estimated using theoretical SEDs from a simulated photometric catalog, created using EGG (Schreiber et al. 2017). The comparison shows that - when the same approach is used to estimate colours, i.e. isophotal magnitudes are adopted - the agreement between the two catalogues is excellent. When we use instead relatively smaller aperture in  $8\times\text{FWHM}$  for the NIRCам photometry we tend to underestimate the F150W and - even more - the F606W flux of the brightest sources, which are considerably more extended than  $8\times\text{FWHM}$ . We ascribe this effect to the existence of colour gradients in bright objects, such that small-sized apertures tend to sample the central, redder part of the galaxies.

From this comparison we conclude that - quite reassuringly - the overall photometric chain is consistent between the well established Frontier Fields data and these new data. At the same time, we remark that the choice of which aperture is optimal depends on the size and kind of objects under study. For faint sources, small apertures tend to have higher S/N and should be preferred. For brightest sources, larger apertures should be preferred. It is also possible to estimate rough color gradients by comparing the various apertures that we release. We also tested that applying the same technique without PSF matching introduces an offset of the order of  $\sim 0.2$  mags in the final colors, which would clearly affect the derived photometric redshifts and SED fitting results.

Finally, in an effort to cross-validate our results prior to release, in the lead up to this paper we compared our catalogs to those under development by the UNCOVER team (Weaver et al. 2023, in prep) based on the same raw datasets. The image processing and photometric procedures adopted by the two teams have significant differences. The main are: i) image coaddition (UNCOVER team adopts GRIZLI, while we use a custom pipeline which uses SCAMP and SWARP; ii) object detection (UNCOVER uses an optimally stacked



**Figure 7.** Comparison of photometry between this work and AstroDeep HST catalogs in the core of the A2744 cluster. *Upper:* Difference between the magnitude in the F160W WFC3 band in AstroDeep and the F150W NIRCам of this work for objects in common between the two catalogues. The F150W magnitude has been corrected for the  $\simeq 0.05$  magnitude shift between the two bands. Filled point represent the difference between magnitudes computed in isophotal areas in both catalogues. Empty points represent the magnitude difference adopting the F150W magnitude computed in  $8\times\text{FWHM}$ . *Bottom:* As above, for the F606W band. The systematic bias between isophotal and  $8\times\text{FWHM}$  colours is due to color gradients in the center of bright sources.

F277W+F356W+F444W image after removing the intracluster light, while we use F444W); iii) techniques and tools for PSF matching and photometry. For these reasons, we expect some differences between the catalogs, especially for faint sources at the detection limit. However, our comparison of working versions of the catalogs produced by the two teams shows overall a good agreement in the colors and magnitudes of the vast majority of objects, with no evidence of significant bias beyond what can be explained by the different choices. We defer a detailed comparison to future versions of the catalog (Stage II).

#### 4. SUMMARY

We present in this paper the data obtained by three NIRCам programs on the A2744 cluster: the GLASS-JWST Early Release Science Program, UNCOVER, and Directory Discretionary Time 2756. All the data, taken with eight different filters (F090W, F115W, F150W, F200W, F277W, F356W, F410M, F444W), have been reduced with an updated pipelines that builds upon the official STScI pipeline but includes a number of improvement to better remove some instrumental signature and streamline the process.

All frames have been aligned onto a common frame with  $0.031''$  pixel scale, approximately matching the na-

tive pixel scale of the short wavelength data. The final images on the whole A2744 region cover an area of 46.5 arcmin<sup>2</sup> with PSF ranging from 0.035" (for the F090W image) to 0.14" (F444W), and reach astonishingly deep  $5\sigma$  magnitude limits from 28.5 to 30.5, depending on location and filter.

We exploit also other HST publicly available programs which have targeted the area, including also the available HST ACS and WFC3 data in the F435W, F606W, F775W and F814W (ACS) and F105W, F125W, F140W and F160W (WFC3) bands, to expand the coverage of the visible-to-IR wavelength range.

On these data we derive a photometric catalog by detecting objects in the F444W image and computing PSF-matched forced photometry on the remaining bands.

We made a number of tests to validate the photometric calibrations, either internal, based on overlapping parts observed in different epochs with different modules, and external, based on cross-correlation with the AstroDeep catalog of the cluster region. They both confirm that photometric offset are limited to at most 0.05 mags or less. Slightly larger (0.1 mags) systematic biases, especially when HST bands are concerned, could be due to the simplified PSF matching that we adopt in this first release.

As we do not explicitly remove the intra-cluster light, photometry of faint sources in the cluster core might also be affected by poor background subtraction.

We publicly release the entire mosaic of the NIRCcam images. The three individual images of each program, which are more homogeneous in terms of PSF orientation and coverage/depth, and potentially more suitable for accurate photometry and for accurate estimate of incompleteness, are also available upon request.

We also publicly release the multi-wavelength catalogue on the entire A2744 area, which includes 24389 objects. We release 5 independent catalogues, based on a different aperture ( $2\times$ ,  $3\times$ ,  $8\times$ ,  $16\times$  the PSF) and in the isophotal area. This catalog is optimized for high redshift galaxies, and in general for faint extragalactic sources, and aimed at allowing a first look at the data and the selection of targets for Cycle 2 proposals. In future releases we plan to include updated calibrations and procedures for the image processing and to optimize the photometry with more sophisticated approaches for PSF matching.

Finally we also release the code developed to remove the  $1/f$  noise from the NIRCcam images, that improves upon the current implementation in the STScI pipeline with a more effective masking of sources in the image.

Images, catalogues and software are immediately available for download from the GLASS-ERS collaboration website<sup>5</sup> and from the ASTRODEEP website<sup>6</sup>. They will also be made available at the MAST archive upon acceptance of the paper.

All the *JWST* data used in this paper can be found in MAST: 10.17909/fqag-p393.

## ACKNOWLEDGEMENT

We warmly thank J. Weaver, K. Withaker, I. Labbè and R. Bezanson for sharing their data with us prior to publication, which made it possible to compare the two processes for data analysis. This work is based on observations made with the NASA/ESA/CSA James Webb Space Telescope, and with the NASA/ESA Hubble Space Telescope. The data were obtained from the Mikulski Archive for Space Telescopes at the Space Telescope Science Institute, which is operated by the Association of Universities for Research in Astronomy, Inc., under NASA contract NAS 5-03127 for *JWST* and NAS 5-26555 for *HST*. These observations are associated with program *JWST*-ERS-1324, *JWST*-DDT-2756, and *JWST*-GO-2561, and several *HST* programs. We acknowledge financial support from NASA through grant *JWST*-ERS-1324. This research is supported in part by the Australian Research Council Centre of Excellence for All Sky Astrophysics in 3 Dimensions (ASTRO 3D), through project number CE170100013. KG and TN acknowledge support from Australian Research Council Laureate Fellowship FL180100060. MB acknowledges support from the Slovenian national research agency ARRS through grant N1-0238. We acknowledge financial support through grants PRIN-MIUR 2017WSCC32 and 2020SKSTHZ. We acknowledge support from the INAF Large Grant 2022 "Extragalactic Surveys with *JWST*" (PI Pentericci). CM acknowledges support by the VILLUM FONDEN under grant 37459. RAW acknowledges support from NASA *JWST* Interdisciplinary Scientist grants NAG5-12460, NNX14AN10G and 80NSSC18K0200 from GSFC. The Cosmic Dawn Center (DAWN) is funded by the Danish National Research Foundation under grant DNR140. This work has made use of data from the European Space Agency (ESA) mission *Gaia* (<https://www.cosmos.esa.int/gaia>), processed by the *Gaia* Data Processing and Analysis Consortium (DPAC, <https://www.cosmos.esa.int/web/gaia/dpac/consortium>). Funding for the DPAC has been provided by national institutions, in particular the institutions participating in the

<sup>5</sup> <https://glass.astro.ucla.edu>

<sup>6</sup> <http://www.astrodeep.eu>

*Gaia* Multilateral Agreement. The authors thank Paola Marrese and Silvia Marinoni (Space Science Data Cen-

ter, Italian Space Agency) for their contribution to the work.

## REFERENCES

- Bertin, E. 2006, in *Astronomical Society of the Pacific Conference Series*, Vol. 351, *Astronomical Data Analysis Software and Systems XV*, ed. C. Gabriel, C. Arviset, D. Ponz, & E. Solano, 112
- Bertin, E., & Arnouts, S. 1996, *A&AS*, 117, 393
- Bertin, E., Mellier, Y., Radovich, M., et al. 2002, in *Astronomical Society of the Pacific Conference Series*, Vol. 281, *Astronomical Data Analysis Software and Systems XI*, ed. D. A. Bohlender, D. Durand, & T. H. Handley, 228
- Bezanson, R., Labbe, I., Whitaker, K. E., et al. 2022, arXiv e-prints, arXiv:2212.04026.  
<https://arxiv.org/abs/2212.04026>
- Boucaud, A., Bocchio, M., Abergel, A., et al. 2016, *A&A*, 596, A63, doi: 10.1051/0004-6361/201629080
- Bouwens, R., Illingworth, G., Oesch, P., et al. 2022, arXiv e-prints, arXiv:2212.06683.  
<https://arxiv.org/abs/2212.06683>
- Castellano, M., Amorín, R., Merlin, E., et al. 2016, *A&A*, 590, A31, doi: 10.1051/0004-6361/201527514
- Castellano, M., Fontana, A., Treu, T., et al. 2022a, arXiv e-prints, arXiv:2207.09436.  
<https://arxiv.org/abs/2207.09436>
- . 2022b, arXiv e-prints, arXiv:2212.06666.  
<https://arxiv.org/abs/2212.06666>
- Ding, X., Silverman, J., Treu, T., et al. 2020, *ApJ*, 888, 37, doi: 10.3847/1538-4357/ab5b90
- Donnan, C. T., McLeod, D. J., Dunlop, J. S., et al. 2023, *MNRAS*, 518, 6011, doi: 10.1093/mnras/stac3472
- Finkelstein, S. L., Bagley, M. B., Arrabal Haro, P., et al. 2022, arXiv e-prints, arXiv:2207.12474.  
<https://arxiv.org/abs/2207.12474>
- Gaia Collaboration, Prusti, T., de Bruijne, J. H. J., et al. 2016, *A&A*, 595, A1, doi: 10.1051/0004-6361/201629272
- Galametz, A., Grazian, A., Fontana, A., et al. 2013, *ApJS*, 206, 10, doi: 10.1088/0067-0049/206/2/10
- Kron, R. G. 1980, *ApJS*, 43, 305, doi: 10.1086/190669
- Merlin, E., Fontana, A., Ferguson, H. C., et al. 2015, *A&A*, 582, A15, doi: 10.1051/0004-6361/201526471
- Merlin, E., Bourne, N., Castellano, M., et al. 2016a, *A&A*, 595, A97, doi: 10.1051/0004-6361/201628751
- Merlin, E., Amorín, R., Castellano, M., et al. 2016b, *A&A*, 590, A30, doi: 10.1051/0004-6361/201527513
- Merlin, E., Fortuni, F., Torelli, M., et al. 2019, *MNRAS*, 490, 3309, doi: 10.1093/mnras/stz2615
- Merlin, E., Castellano, M., Santini, P., et al. 2021, *A&A*, 649, A22, doi: 10.1051/0004-6361/202140310
- Merlin, E., Bonchi, A., Paris, D., et al. 2022, *A&A*, 938, L14, doi: 10.3847/2041-8213/ac8f93
- Morishita, T., & Stiavelli, M. 2022, arXiv e-prints, arXiv:2207.11671. <https://arxiv.org/abs/2207.11671>
- Naidu, R. P., Oesch, P. A., van Dokkum, P., et al. 2022, arXiv e-prints, arXiv:2207.09434.  
<https://arxiv.org/abs/2207.09434>
- Nardiello, D., Bedin, L. R., Burgasser, A., et al. 2022, *MNRAS*, 517, 484, doi: 10.1093/mnras/stac2659
- Oke, J. B., & Gunn, J. E. 1983, *ApJ*, 266, 713, doi: 10.1086/160817
- Rigby, J., Perrin, M., McElwain, M., et al. 2022, arXiv e-prints, arXiv:2207.05632.  
<https://arxiv.org/abs/2207.05632>
- Roberts-Borsani, G., Treu, T., Chen, W., et al. 2022, arXiv e-prints, arXiv:2210.15639.  
<https://arxiv.org/abs/2210.15639>
- Robertson, B. E., Tacchella, S., Johnson, B. D., et al. 2022, arXiv e-prints, arXiv:2212.04480.  
<https://arxiv.org/abs/2212.04480>
- Schlawin, E., Leisenring, J., Misselt, K., et al. 2020, *AJ*, 160, 231, doi: 10.3847/1538-3881/abb811
- Schreiber, C., Pannella, M., Leiton, R., et al. 2017, *A&A*, 599, A134, doi: 10.1051/0004-6361/201629155
- Treu, T., Roberts-Borsani, G., Bradac, M., et al. 2022, *ApJ*, 935, 110, doi: 10.3847/1538-4357/ac8158
- Yan, H., Cohen, S. H., Windhorst, R. A., et al. 2022, arXiv e-prints, arXiv:2209.04092.  
<https://arxiv.org/abs/2209.04092>